UCLA
UCLA Previously Published Works

Title

Magnetic Field Annihilation in a Magnetotail Electron Diffusion Region With Electron-Scale Magnetic Island

Permalink

Journal

ISSN

Authors

Hasegawa, H
Denton, RE
Nakamura, TKM
et al.

Publication Date

DOI

JGR Space Physics

Correspondence to:
H. Hasegawa,
hase@stp.isas.jaxa.jp

Magnetic Field Annihilation in a Magnetotail Electron Diffusion Region With Electron-Scale Magnetic Island

H. Hasegawa[1] , R. E. Denton[2] , T. K. M. Nakamura[3,4] , K. J. Genestreti[5] , T. D. Phan[6],
R. Nakamura[3] , K.-J. Hwang[7] , N. Ahmadi[8] , Q. Q. Shi[9] , M. Hesse[10] ,
J. L. Burch[7] , J. M. Webster[7] , R. B. Torbert[4,11] , B. L. Giles[12] , D. J. Gershman[12] ,
C. T. Russell[13] , R. J. Strangeway[13] , H. Y. Wei[13] , P.-A. Lindqvist[14] , Y. V. Khotyaintsev[15] ,
R. E. Ergun[16] , and Y. Saito[1]

[1]Institute of Space and Astronautical Science, Japan Aerospace Exploration Agency, Sagamihara, Japan, [2]Department of Physics and Astronomy, Dartmouth College, Hanover, NH, USA, [3]Space Research Institute, Austrian Academy of Sciences, Graz, Austria, [4]Institute of Physics, University of Graz, Graz, Austria, [5]Southwest Research Institute, Durham, NH, USA, [6]Space Sciences Laboratory, University of California, Berkeley, CA, USA, [7]Southwest Research Institute, San Antonio, TX, USA, [8]Laboratory for Atmospheric and Space Physics, University of Colorado, Boulder, CO, USA, [9]Shandong Provincial Key Laboratory of Optical Astronomy and Solar-Terrestrial Environment, Institute of Space Sciences, Shandong University, Weihai, China, [10]NASA Ames Research Center, Moffett Field, CA, USA, [11]Physics Department, University of New Hampshire, Durham, NH, USA, [12]NASA Goddard Space Flight Center, Greenbelt, MD, USA, [13]Department of Earth, Planetary, and Space Sciences, University of California, Los Angeles, CA, USA, [14]Royal Institute of Technology, Stockholm, Sweden, [15]Swedish Institute of Space Physics, Uppsala, Sweden, [16]Department of Astrophysical and Planetary Sciences, University of Colorado, Boulder, CO, USA

Abstract We present observations in Earth's magnetotail by the Magnetospheric Multiscale spacecraft that are consistent with magnetic field annihilation, rather than magnetic topology change, causing fast magnetic-to-electron energy conversion in an electron-scale current sheet. Multi-spacecraft analysis for the magnetic field reconstruction shows that an electron-scale magnetic island was embedded in the observed electron diffusion region (EDR), suggesting an elongated shape of the EDR. Evidence for the annihilation was revealed in the form of the island growing at a rate much lower than expected for the standard X-type geometry of the EDR, which indicates that magnetic flux injected into the EDR was not ejected from the X-point or accumulated in the island, but was dissipated in the EDR. This energy conversion process is in contrast to that in the standard EDR of a reconnecting current sheet where the energy of antiparallel magnetic fields is mostly converted to electron bulk-flow energy. Fully kinetic simulation also demonstrates that an elongated EDR is subject to the formation of electron-scale magnetic islands in which fast but transient annihilation can occur. Consistent with the observations and simulation, theoretical analysis shows that fast magnetic diffusion can occur in an elongated EDR in the presence of nongyrotropic electron effects. We suggest that the annihilation in elongated EDRs may contribute to the dissipation of magnetic energy in a turbulent collisionless plasma.

Plain Language Summary Magnetic reconnection in electric current sheets is the key to fast release of magnetic energy in many space and astrophysical plasma systems, such as during magnetospheric substorms and solar flares. Establishing the mechanism by which magnetic energy is converted to particle energy in the reconnection process is the key to understanding the large-scale impacts of reconnection, including energy partition and particle acceleration. It is generally believed that an electron-scale diffusion region (EDR), where a magnetic-to-electron energy conversion occurs, has an X-type magnetic field geometry around which the energy of antiparallel magnetic fields injected into the EDR is mostly converted to the bulk-flow energy of electrons by magnetic tension of reconnected field lines. Contrary to this standard X-type magnetic field geometry of reconnection, we report observations in Earth's magnetotail by NASA's Magnetospheric Multiscale spacecraft showing that the EDR can be highly elongated. The important and surprising consequence of the observed elongated shape of the EDR is that the fast energy conversion in the EDR can be caused mostly by magnetic field annihilation, rather than magnetic topology change. The fast collisionless annihilation that we discovered is fundamentally different from the classical magnetic field annihilation due to collisional and wave-induced resistivity.

Genestreti, T. D. Phan, R. Nakamura,
K.-J. Hwang, J. M. Webster
Methodology: H. Hasegawa, R. E.
Denton
Project Administration: J. L. Burch, R.
B. Torbert, B. L. Giles
Software: H. Hasegawa, R. E. Denton,
Q. Q. Shi
Validation: H. Hasegawa, R. E. Denton,
T. K. M. Nakamura
Visualization: T. K. M. Nakamura
Writing – original draft: H. Hasegawa
Writing – review & editing: R. E.
Denton, T. K. M. Nakamura, K. J.
Genestreti, T. D. Phan, R. Nakamura,
K.-J. Hwang, J. L. Burch, C. T. Russell

1. Introduction

Magnetic reconnection in Earth's magnetotail is fast, with an inflowing plasma speed of ~ 0.1 times the Alfvén speed in the inflow region, and has large-scale impacts, for example, explosive release of magnetic energy during magnetospheric substorms (Angelopoulos et al., 2008; Nagai et al., 2011). Magnetotail reconnection occurs under such simple boundary conditions that on the two sides of the current sheet the magnetic field is approximately oppositely directed with a comparable intensity, and plasmas have similar densities and temperatures. Such nearly antiparallel and symmetric reconnection is ideal for studying intrinsic properties of magnetic reconnection in the collisionless regime.

In the standard model of reconnection, the electron diffusion region (EDR), where the "frozen-in condition" is violated for both ions and electrons, is localized with an X-type field geometry where a magnetic-to-electron energy conversion occurs by changing the magnetic field topology (Torbert et al., 2018). It is generally accepted that in such EDRs most of the energy of antiparallel magnetic fields injected by the inflow is converted to bulk-flow energy of electrons ejected into the regions downstream of the EDR (Shay et al., 2007), called the exhausts, by magnetic tension (Lorentz force) of reconnected field lines. Numerical simulations suggest that the EDR may be elongated in the outflow direction to form a planar geometry (Daughton et al., 2006; Fujimoto, 2006), and an elongated EDR is subject to the formation of electron-scale magnetic islands, likely through the electron tearing instability (Nakamura et al., 2021). The conventional wisdom is that the elongation of the EDR results in a substantial reduction of the reconnection rate (Daughton et al., 2006; Fujimoto, 2006). However, a fully kinetic simulation by Nakamura et al. (2021) shows that the reconnection rate defined as the rate of in-plane magnetic flux injection to the dominant X-point can remain high (~ 0.1 in dimensionless units) even during the phase when the EDR is elongated (see their Figure 2d), and suggests that fast energy conversion can be sustained by magnetic field annihilation, rather than field topology change, for about one ion cyclotron period.

Figure 1 shows the time evolution of the in-plane magnetic field and energy conversion rate in and around the EDR for time $t = 55.4\Omega_i^{-1}$ to $56.2\Omega_i^{-1}$, seen in the two-dimensional (2-D) simulation reported by Nakamura et al. (2021). Here, Ω_i is ion gyrofrequency, and the ion to electron mass ratio is 400 (see Text S1 in Supporting Information S1 for details of the simulation settings). The energy conversion rate $\mathbf{j} \cdot (\mathbf{E} + \mathbf{v}_e \times \mathbf{B})$ is significantly positive in the electron-scale current sheet throughout the interval, indicating that significant magnetic-to-particle energy conversion continuously occurs there. This is consistent with the fact that the minimum of partial magnetic vector potential (flux function) A_M, corresponding to A_M at the most dominant X-point, continuously decreases with time (Figure 1f), because $\partial A_M / \partial t = -E_M$ (see Figure 2d of Nakamura et al. (2021) for the actual time evolution of E_M). In 2-D, the motion of a specific magnetic field line can be tracked by tracing the location of equal vector potential values A_M in time. In the absence of magnetic field annihilation, A_M at the O-point, which corresponds to the center of magnetic islands and can be identified as a local A_M maximum in Figure 1f, should be constant in time. This is because in such cases the in-plane magnetic flux injected to the X-point would be reconnected, ejected toward the exhausts, and accumulated in the island. This is roughly the case when the island size is near or larger than the ion inertial length ($d_{i0} = 20d_{e0}$), as seen in Figures 1d and 1e for $t = 56.0\Omega_i^{-1}$ to $56.2\Omega_i^{-1}$ when $\mathbf{j} \cdot (\mathbf{E} + \mathbf{v}_e \times \mathbf{B})$ is nearly zero around the O-point.

On the other hand, A_M at the O-point continuously decreases from $t = 55.4\Omega_i^{-1}$ to $56.0\Omega_i^{-1}$ when $\mathbf{j} \cdot (\mathbf{E} + \mathbf{v}_e \times \mathbf{B})$ is significantly positive not only at the X-point but also around the O-point. Note that an electron-scale magnetic island is formed already at $t = 55.4\Omega_i^{-1}$ when the EDR is elongated (very small local maximum in red curve of Figure 1f at $L/d_{e0} \sim 1019$; see also Figure 3f of Nakamura et al. (2021)). The continuous A_M decrease at the O-point is evidence from the simulation that the annihilation of in-plane magnetic field is occurring in the electron-scale island. At present, it remains unclear whether the annihilation of B_L around the X-point or that of B_N around the O-point is dominant. Thus, the annihilation in the present study may be defined as non- or weak-ejection of in-plane magnetic flux out of the X-point due to B_L diffusion, or diffusion of the reconnected field component B_N at the O-point, under the presence of significant E_M. It is probable, however, that the electron-scale annihilation is mostly due to that of B_L because the diffusion process is more efficient in regions where the gradient of the corresponding quantity (in-plane magnetic field in the present case) is larger (see also Section 4).

Since the collisionless magnetic field annihilation on the electron scale has only recently been identified in simulation (Nakamura et al., 2021), it remains unknown if such a process can actually occur in spatially extended
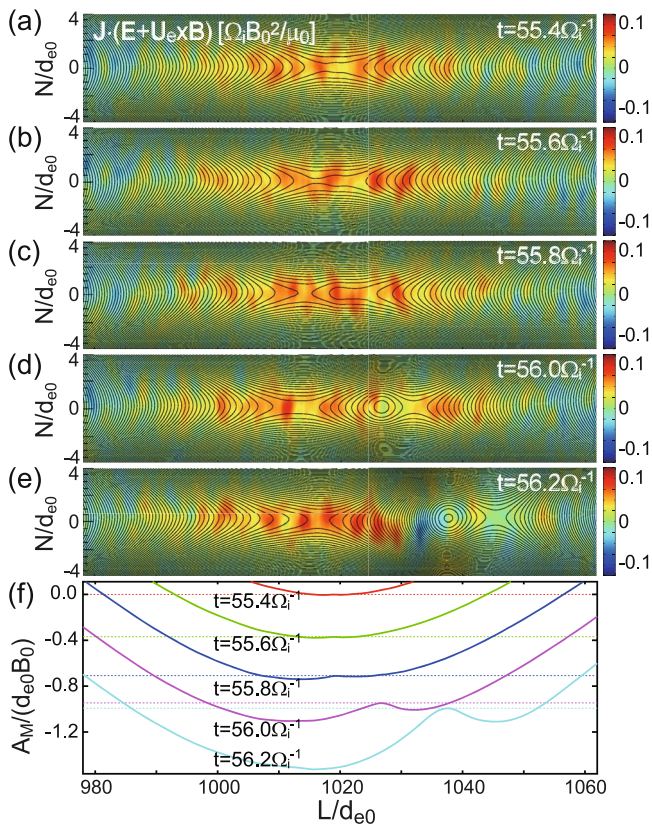
Figure 1. (a–e) Time evolution of an electron diffusion region (EDR) from a fully kinetic simulation of turbulent magnetic reconnection (Nakamura et al., 2021), showing EDR elongation and island growth on the scale of electron inertial length d_{e0}. In-plane magnetic field lines are shown by black curves and energy conversion rate $\mathbf{j} \cdot (\mathbf{E} + \mathbf{v}_e \times \mathbf{B})$ (Zenitani et al., 2011) in color, where $\mathbf{E}$ and $\mathbf{B}$ are the electric and magnetic fields, respectively, $\mathbf{j}$ current density, and $\mathbf{v}_e$ electron flow velocity. (f) Simulated vector potential (flux function) A_M along $N = 0$ for selected times. It shows that A_M at the O-point (local A_M maximum, marked by the horizontal dashed lines) continuously decreases from $t = 55.4\Omega_i^{-1}$ to $56.0\Omega_i^{-1}$ at a rate comparable to that at the primary X-point (A_M minimum), demonstrating that magnetic field annihilation occurs in and around the island. In the simulation, A_M is computed by setting A_M at the N boundaries, which are conducting walls located at $N = \pm 20d_{i0} = \pm 400d_{e0}$, to have a fixed value for all times. In panel (f), however, A_M is defined to be zero at the O-point (local A_M maximum on $N = 0$) at $t = 55.4\Omega_i^{-1}$ for brevity.

EDRs with negligibly small reconnected field components in space. This is also because unambiguous identification of EDR structures in space requires high-spatiotemporal-resolution plasma measurements, and there has been no data analysis method to distinguish whether the magnetic field injected into the EDR is reconnected or annihilated.

In this paper, we present an in-depth analysis of the fortuitous multi-spacecraft observations by the Magnetospheric Multiscale (MMS) mission (Burch et al., 2016) of a magnetotail EDR and electron-scale magnetic island on 10 August 2017 (Zhou et al., 2019), in which the magnetic-to-particle energy conversion rate was consistent with fast reconnection. Contrary to the standard model of the EDR with an X-type field geometry, however, our analysis suggests that the EDR was elongated in the outflow direction and the fast energy conversion observed in the EDR was supported by magnetic field annihilation, rather than magnetic topology change. Consistent with this interpretation, our theoretical analysis shows that fast magnetic diffusion can occur in an elongated EDR in the presence of nongyrotropic electron effects, and may lead to magnetic field annihilation within electron-scale islands.

2. Overview of the Observations

For this study, MMS burst-mode data from the following instrument suites were used: FIELDS (Torbert et al., 2016), including the electric field instruments (Ergun et al., 2016; Lindqvist et al., 2016) and magnetometers (Russell et al., 2016), and Fast Plasma Investigation (FPI) for electron and ion plasma distributions and moments (Pollock et al., 2016).

In Figures 2a–2d, we show the context of the reconnecting current sheet observed by the MMS2 spacecraft on 10 August 2017 at 12:17:40–12:19:40 UT, when MMS was fully embedded in the hot magnetotail plasma sheet (Zhou et al., 2019) at $(-15.2, 4.6, 3.1)$ R_E in GSM coordinates. The current sheet at 12:18:30 UT is characterized by a reversal from anti-sunward to sunward ion flows (negative to positive v_{ix} change in Figure 2b), crossing from its southern to northern side (negative to positive B_x change in Figure 2a). The ion flow speeds around the start and end of the interval are comparable to the ion Alfvén speed $V_{iA} = B/(\mu_0\rho)^{1/2} \approx 850$ km s^{-1} based on the magnetic field intensity $B \approx 15$ nT and proton number density of 0.15 cm^{-3}, where μ_0 is the vacuum permeability and ρ is plasma mass density. A fast dawnward electron flow ($v_{ey} \approx -10$ Mm s^{-1} in Figure 2c) and a relatively slow duskward ion flow with no enhancement at the current sheet show that its electric current was supported by electrons. These features indicate that MMS crossed an electron-scale current sheet (ECS) embedded inside a region of large-scale reconnection when traversing from its anti-sunward exhaust to sunward exhaust. Earlier studies of this current sheet (Li et al., 2019; Zhou et al., 2019) reported established signatures of EDRs (Burch et al., 2016; Torbert et al., 2018), including oppositely directed electron jets with a speed exceeding V_{iA} (Figure 2c), crescent-shaped electron velocity distributions, and magnetic-to-particle energy conversion.

3. Reconstruction of the Electron-Scale Current Sheet

We investigate the ECS structure in detail by the use of two sophisticated data analysis techniques that can reconstruct multi-dimensional magnetic field structures in regions around the spacecraft from in situ measurements of the magnetic field and plasma bulk parameters. One is a single-spacecraft method based on electron-magnetohydrodynamics (EMHD) equations that can recover quasi-steady, two-dimensional (2-D)
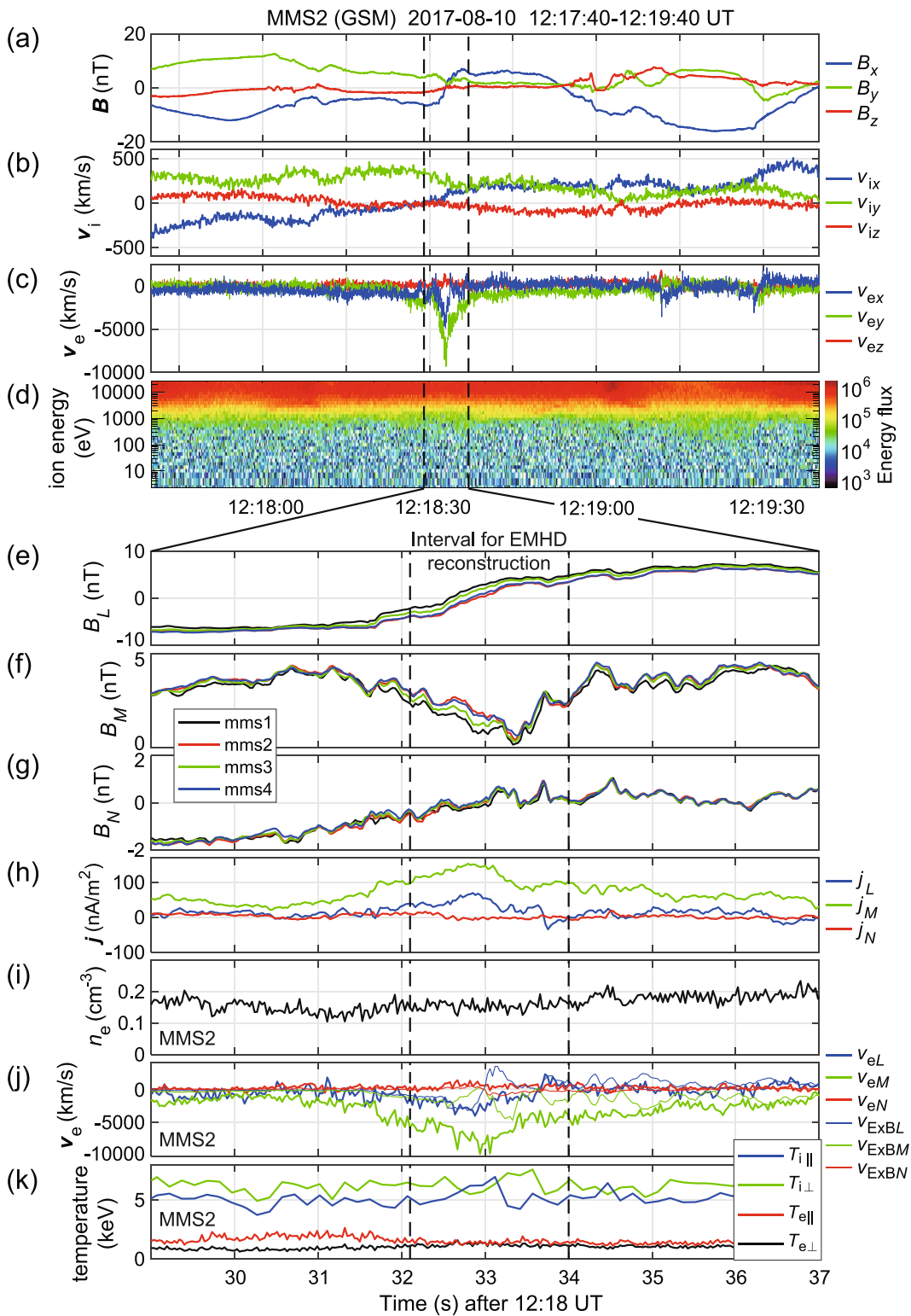
Figure 2.

magnetic, electrostatic, and electron velocity fields around the path of the observing spacecraft, hereafter called EMHD reconstruction (Hasegawa et al., 2021; Sonnerup et al., 2016; Text S2 in Supporting Information S1). The other is a multi-spacecraft method based on polynomial (second-order Taylor) expansion of the magnetic field that can recover three-dimensional (3-D) magnetic field using instantaneous measurements by the four spacecraft

of the magnetic field and particle current density, called polynomial reconstruction (Denton et al., 2020; Text S3 in Supporting Information S1).

3.1. Dimensionality of the Structure

To analyze the dimensionality of the ECS, the Maximum Directional Derivative (MDD) method (Shi et al., 2019) was applied to four-spacecraft measurements of the magnetic field for an interval 12:18:29–12:18:37 UT surrounding the reconstruction interval (Figure 3). The square roots of the resulting eigenvalues, as shown in Figure 3e, represent the estimated magnitude of magnetic gradient in the direction of the corresponding eigenvectors. Therefore, Figure 3e shows that the gradient along the eigenvector corresponding to the maximum eigenvalue λ_{max} and thus to the current sheet normal is much larger than the gradients along the other two eigenvalues. Figure 3f shows that the first dimension number index D_1 (Rezeau et al., 2018) is much larger than the other two indices (see the Figure 3 caption for the definition of those indices). These results suggest that the magnetic structure of the ECS was locally nearly one-dimensional during the reconstruction interval. Figure 3g shows that $\mathbf{k}_{max}$, which can be taken as the ECS normal direction, was stably northward throughout the reconstruction interval. These results indicate that the ECS was approximately planar with no significant undulation on the scale of the spacecraft separation ∼18 km which was comparable to the electron inertial length ($d_e \sim 14$ km). The fact that λ_{mid} is somewhat larger than λ_{min} (Figure 3e) suggests that although the ECS was nearly one-dimensional, there were some 2-D structures that may be recovered by the EMHD reconstruction.

3.2. Data in the LMN Coordinate System

Figures 2e–2k show the magnetic field and plasma data from MMS, used as input for the two reconstruction techniques, in a current-sheet ("LMN") coordinate system: the current-sheet normal points along **N** (roughly northward in the magnetotail), the reconnecting antiparallel magnetic field component is along **L** (roughly sunward), and **M** = **N** × **L** is along the "X-line" direction (roughly duskward). The final LMN coordinate system used in this study (Figure 2 caption) was determined through optimization of the EMHD reconstruction results, as detailed in Section 3.4. A preliminary LMN coordinate system used as trial LMN axes in the reconstruction was determined by a hybrid method (Denton et al., 2018), which combines the Maximum Variance Analysis (MVA) of the magnetic field (Sonnerup & Scheible, 1998) and Maximum Directional Derivative (MDD) method (Shi et al., 2019) applied to four-spacecraft measurements of the magnetic field at 12:18:31–12:18:36 UT. The resulting LMN axes are: $\mathbf{L}_p = (0.992, -0.127, -0.022)_{GSM}$, $\mathbf{M}_p = (0.127, 0.992, -0.003)_{GSM}$, and $\mathbf{N}_p = (0.022, -0.000, 1.000)_{GSM}$, which are not very different from the final axes.

A weak guide field (∼2 nT) (Zhou et al., 2019), the component (B_M) along the X-line of the magnetic field external to the entire larger-scale current sheet, or, in this case, at the center of the ECS (Figure 2f), confirms that reconnection occurred under nearly antiparallel magnetic field conditions. Negative to positive variation of B_N (Figure 2g) is consistent with MMS moving from the anti-sunward to sunward side of the reconnection site; the X-line was moving anti-sunward (Section 3.3). The assumptions of constant density and isotropic electron temperature made in the EMHD reconstruction are approximately satisfied for an intense current density interval at 12:18:32.1–12:18:34.0 UT (Figures 2i and 2k) to which the method is applied.

3.3. Frame Velocity

The EMHD reconstruction is performed in a frame of reference commoving with the structure. It was estimated by a multi-spacecraft data-analysis technique known as the spatiotemporal difference (STD) method (Shi

Figure 2. Overview of Magnetospheric Multiscale (MMS) observations of an electron-scale current sheet with both ion and electron reconnection jet signatures. (a–d) GSM components of the magnetic field (a; B_x, B_y, and B_z), ion velocity (b; v_{ix}, v_{iy}, and v_{iz}), electron velocity (c; v_{ex}, v_{ey}, and v_{ez}) and ion energy-time spectrogram of omni-directional differential energy flux ((d); color scale, in units of keV s^{-1} cm^{-2} sr^{-1} keV^{-1}) seen by MMS2. (e–h) Components in a common current-sheet (LMN) coordinate system of the magnetic field (e.g., B_L, B_M, and B_N) from all four spacecraft (black, MMS1; red, MMS2; green, MMS3; blue, MMS4) and current density $\mathbf{j} = (\nabla \times \mathbf{B})/\mu_0$ (Dunlop et al., 2002) ((h) j_L, j_M, and j_N). (i–k) MMS2 measurements of the electron density ((i) n_e), electron velocity and electric drift velocity $(\mathbf{E} \times \mathbf{B})/B^2$ in LMN coordinates ((j) v_{eL}, v_{eM}, v_{eN}, v_{ExBL}, v_{ExBM}, and v_{ExBN}), and ion and electron temperatures ((k) T_i and T_e) in the directions parallel (∥) and perpendicular (⊥) to the local magnetic field. GSM components of the LMN axes are: **L** = (0.955, −0.298, −0.021), **M** = (0.296, 0.953, −0.059), and **N** = (0.038, 0.050, 0.998) (Section 3.2).
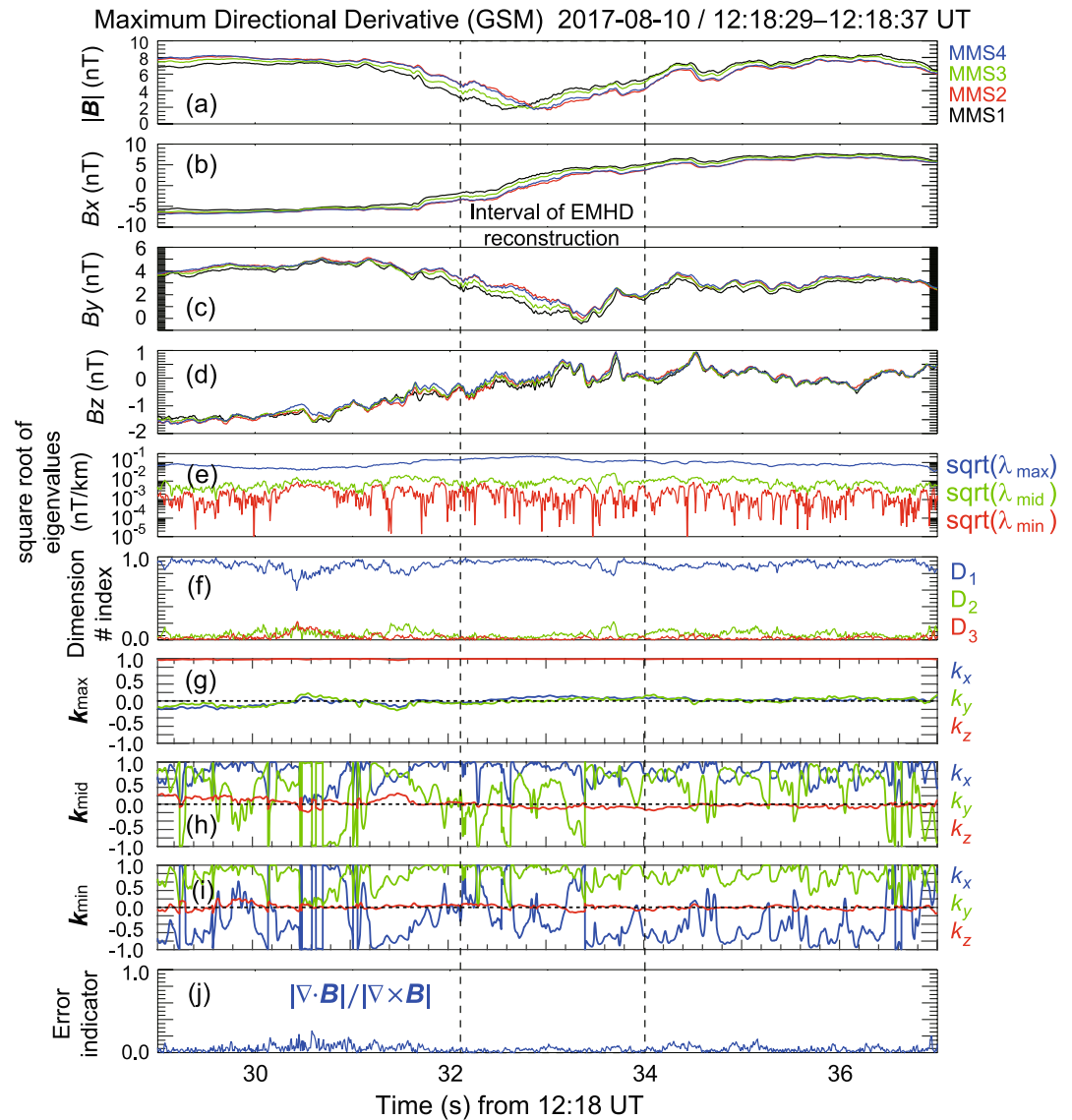
Figure 3. Results from the Maximum Directional Derivative method (Shi et al., 2019) applied to an interval 12:18:29–12:18:37 UT. (a–d) GSM components of the magnetic field measured by the four Magnetospheric Multiscale (MMS) spacecraft ((a) $|\mathbf{B}|$, (b) B_x, (c) B_y, and (d) B_z). (e) Square roots of the maximum, intermediate, and minimum eigenvalues (λ_{max}, λ_{mid}, and λ_{min}) of the 3×3 Maximum Directional Derivative matrix (Shi et al., 2019). (f) Dimension number indices (Rezeau et al., 2018), defined as $D_1 = (\lambda_{max} - \lambda_{mid})/\lambda_{max}$, $D_2 = (\lambda_{mid} - \lambda_{min})/\lambda_{max}$, and $D_3 = \lambda_{min}/\lambda_{max}$, that can be used as measures of the dimensionality of the structure encountered by the spacecraft. (g–i) Eigenvectors corresponding to the three eigenvalues ((g) $\mathbf{k}_{max}$; (h) $\mathbf{k}_{mid}$; (i) $\mathbf{k}_{min}$). (j) $|\nabla \cdot \mathbf{B}|/|\nabla \times \mathbf{B}|$ as an error proxy.

et al., 2019), applied to smoothed magnetic field data from the four spacecraft at 12:18:32.0–12:18:33.3 UT. The velocity component from the STD method along the minimum magnetic-gradient direction $\mathbf{k}_{min}$, which is often along $\mathbf{M}$ (Figure 3i), is usually unreliable (Denton et al., 2016) and was not used. The resulting velocity is $\mathbf{V}_{STD} = -100\mathbf{L}_p - 28\mathbf{N}_p$ km s^{-1}, consistent with an anti-sunward moving EDR and south-to-north crossing of the ECS. The normal velocity roughly agrees well with that (-35 km s^{-1}) estimated by multi-spacecraft timing analysis (Zhou et al., 2019). The L-component dominated motion of the structure, combined with the approximately planar geometry of the ECS (Figure 3f), indicates that the ECS was elongated in the outflow direction. The L and N components of the final structure velocity $\mathbf{V}_{str} = (-30, 237, -40)_{GSM}$ km s^{-1}, used in the EMHD reconstruction, are the projections along $\mathbf{L}$ and $\mathbf{N}$ of $\mathbf{V}_{STD}$ and the M component ($V_{str,M}$) is that of the mean ion velocity for the reconstruction interval, so that the electric current is supported mostly by electrons in the structure frame.
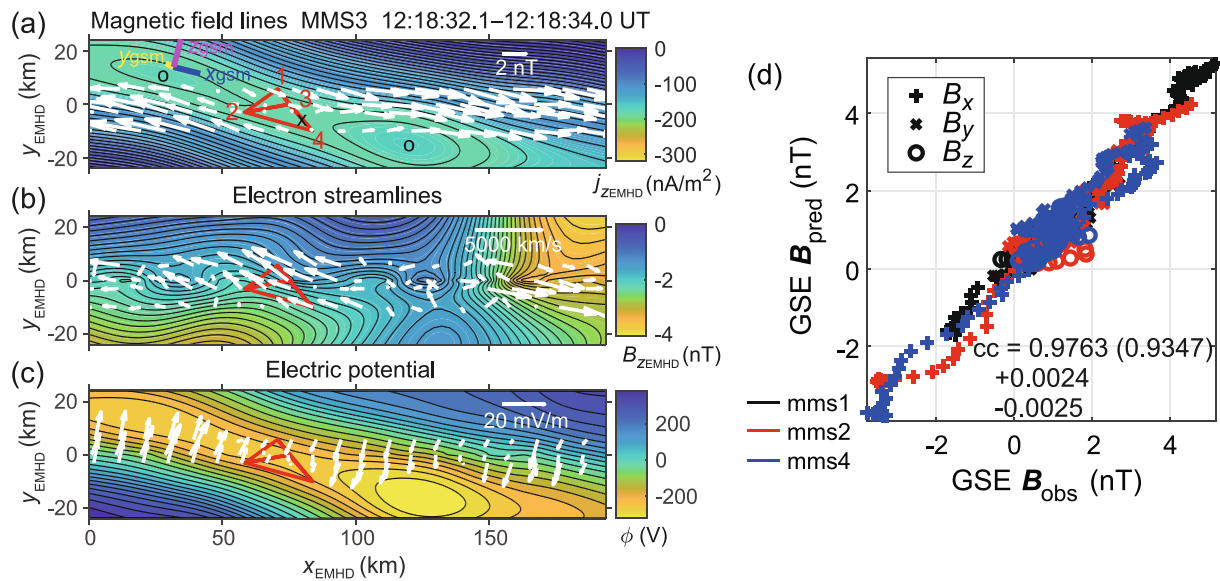
Figure 4. 2-D magnetic, electrostatic, and electron-velocity fields recovered from the electron-magnetohydrodynamics reconstruction applied to the Magnetospheric Multiscale (MMS) 3 data at 12:18:32.1–12:18:34.0 UT. (a) Reconstructed in-plane magnetic field-lines with the out-of-plane component ($j_{z,EMHD}$) of the reconstructed current density in color. White arrows show the projections onto the reconstruction plane of the measured magnetic fields along the paths (y_{EMHD} = const.) of the four spacecraft. (b) Reconstructed electron streamlines with the out-of-plane component ($B_{z,EMHD}$) of the reconstructed magnetic field in color. The arrows show the projections of the measured electron velocities transformed into the structure-rest frame. (c) Reconstructed electrostatic potential (ϕ), along with the projections of the measured electric field ($\mathbf{E}_{str} = \mathbf{E} + \mathbf{V}_{str} \times \mathbf{B}$) transformed into the structure-rest frame. (d) Correlation between the components in geocentric solar ecliptic (GSE) coordinates of the measured magnetic field (B_x: plus, B_y: cross, and B_z: circle) and those predicted from the reconstruction along the paths of MMS 1 (black), MMS 2 (red), and MMS 4 (blue) not used as input for the reconstruction. The bootstrap method (Kawano & Higuchi, 1995) was used to estimate the confidence intervals of the correlation coefficients corresponding to ± 1 sigma. The value in the parenthesis is the correlation coefficient between the values measured by MMS3 (used as input for the reconstruction) and those measured during the same interval by the other three spacecraft, with an aim to demonstrate whether the reconstruction provides better prediction along the paths of the other three spacecraft.

3.4. EMHD Reconstruction

Figure 4 shows the magnetic field, electron streamlines, and electric field reconstructed for the present ECS from the EMHD reconstruction technique including electron inertia effects but assuming incompressibility (i.e., constant density) (Hasegawa et al., 2021). The input data were taken during a 1.9 s interval 12:18:32.1–12:18:34.0 UT from MMS3, which was located near the centroid of the MMS tetrahedron in the reconstruction plane. The final LMN axes were optimized by a multi-spacecraft method (Hasegawa et al., 2019), which searches for the invariant-axis ($\hat{z}_{EMHD}$) orientation that maximizes the correlation coefficient (Figure 4d) between the normalized components of the magnetic field and electron velocity measured by three spacecraft not used as input in the reconstruction and those predicted at points along the paths of the three spacecraft from the reconstructed field maps. The reconstruction axes thus determined are: $\hat{x}_{EMHD} = (0.927, -0.271, 0.260)_{GSM}$, $\hat{y}_{EMHD} = (-0.232, 0.131, 0.964)_{GSM}$, and $\hat{z}_{EMHD} = (-0.296, -0.953, 0.059)_{GSM}$.

The reconstructed streamlines (Figure 4b) clearly show the inflow and outflow patterns as expected for 2D reconnection but have a complex structure, probably because of the presence of an electron-scale magnetic island (Figure 4a), and time evolution associated with its growth (Figure 5). Note, however, that a quadrupolar pattern of $B_{z,EMHD} = -B_M$ related to the Hall effect (Nagai et al., 2001; Øieroset et al., 2001) is roughly reconstructed. The electron stagnation point appears to be located near the O-point, rather than the X-point. Such a displacement in the outflow direction of the X and stagnation point has been observed for another magnetotail EDR event reported by Torbert et al. (2018) (Hasegawa et al., 2019).

Figure 4d shows that the magnetic field is well reconstructed with a very high correlation coefficient, which suggests that the reconstruction coordinate system is well determined. We emphasize that the correlation coefficient between the predicted and measured components is significantly larger than that between the input values recorded by MMS3 and those recorded by the other three spacecraft for the same interval and interpolated to the instants of the MMS3 measurements (value in the parenthesis in Figure 4d). The spacecraft separation ~18 km
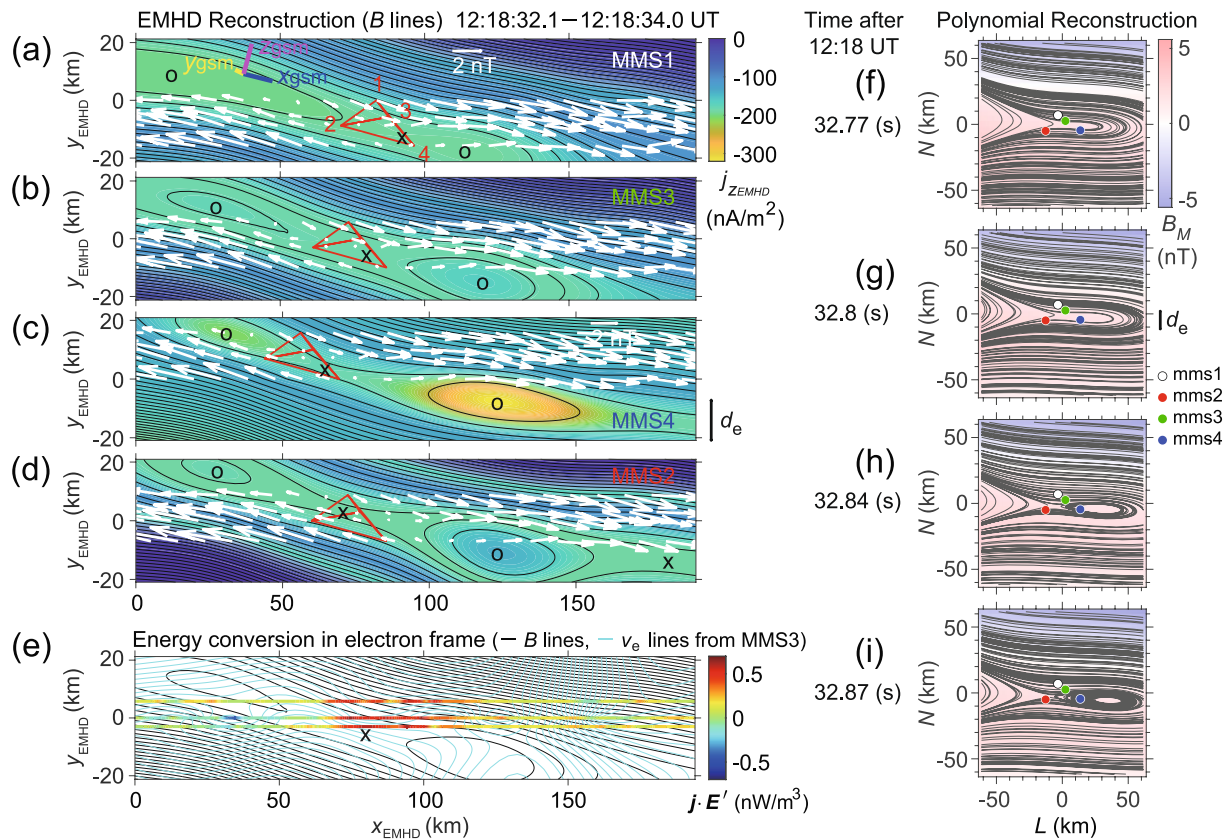
Figure 5. Magnetic fields recovered from the electron-magnetohydrodynamics (EMHD) and polynomial reconstruction methods (Texts S2 and S3 in Supporting Information S1). (a–d) 2-D magnetic fields from the EMHD reconstruction with electron inertia effects (Hasegawa et al., 2021) using the data taken at 12:18:32.1–12:18:34.0 UT individually for each of the four spacecraft, shown in the order of current sheet crossing (Magnetospheric Multiscale (MMS1), (a) MMS3, (b) MMS4, (c) then MMS2, (d) as seen in Figure 2e). Black curves show the reconstructed magnetic field-lines, colors the out-of-plane component ($j_{z,\mathrm{EMHD}}$) of the reconstructed current density, and white arrows the projections onto the reconstruction ($x_{\mathrm{EMHD}} - y_{\mathrm{EMHD}}$) plane of the measured magnetic fields along the paths of the four spacecraft. The bars near the upper-left corner of panel (a) are the projections of the unit GSM axes (blue, $\hat{\mathbf{x}}_{\mathrm{GSM}}$; yellow, $\hat{\mathbf{y}}_{\mathrm{GSM}}$; magenta, $\hat{\mathbf{z}}_{\mathrm{GSM}}$). (e) Magnetic field lines (black curves) and electron streamlines (blue curves) reconstructed from the MMS 3 data, with $\mathbf{j}_p \cdot \mathbf{E}'$ (Zenitani et al., 2011) measured along the paths of MMS 1, MMS 2, and MMS 3 in color. (f–i) Projection onto the L–N plane of 3D magnetic field-lines reconstructed using the polynomial reconstruction (Denton et al., 2020) from instantaneous measurements by the four spacecraft of $\mathbf{B}$ and $\mathbf{j}_p$, with reconstructed B_M in color.

was comparable to the island thickness of order $d_e \sim 14$ km. Thus, the high correlation suggests that we may rely on the reconstructed magnetic fields on those spatial scales.

3.5. Comparison Among the Four Spacecraft and With Polynomial Reconstruction

Figure 5 shows the 2-D representation of the magnetic field reconstructed from the EMHD and polynomial reconstructions (Text S3 in Supporting Information S1). Both reconstruction results (Figures 5a–5d and 5f–5i) clearly show that an electron-scale magnetic island was forming and growing in the ECS with a thickness of about one d_e. This is consistent with the MDD result suggesting that the ECS had a planar and elongated configuration (Figure 3), ideal for island generation (Daughton et al., 2006). The island size in the L direction may look shorter than the fastest growing wavelength (of order 10 d_e) of the electron tearing instability (Jain & Sharma, 2015), but note that such small islands have been seen in kinetic simulations (Figure 3 of Nakamura et al., 2021).

Figures 5a–5d show that over a ~0.4 s interval of 12:18:32.6–12:18:33.0 UT, during which the current sheet was crossed in the order of MMS 1, MMS 3, MMS 4, and MMS 2 (Figure 2e), both the length (along $\mathbf{L}$) and width (along $\mathbf{N}$) of the island grew. An entirely consistent feature is seen in Figures 5f–5i. The timescale (~0.4) of the ECS crossing is comparable to the proton cyclotron period, so that the island growth was probably slow on the electron time scale. This feature is further confirmed by slow accumulation of in-plane magnetic flux in the island (Figure 6); the quasi-steady assumption of the EMHD reconstruction is approximately satisfied.
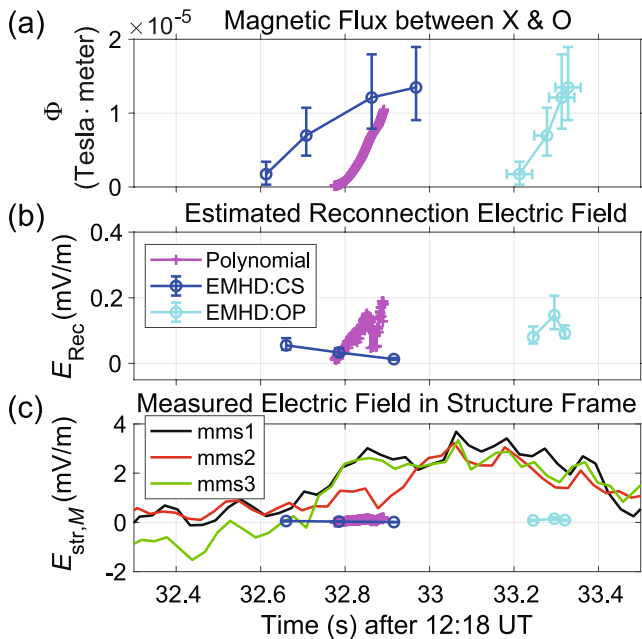
Figure 6. Reconnection electric fields, estimated from the electron-magnetohydrodynamics (EMHD) and polynomial reconstructions, compared with the measured electric field. (a) In-plane magnetic flux (Φ) embedded between the X- and O-points around the center of the reconstruction domain as a function of time. For the EMHD reconstruction, blue circles show the case when time is tagged by that of current sheet crossing ($B_L = 0$) by each spacecraft, while cyan circles show the case when time is tagged by that of closest approach to the reconstructed O-point. (b) Rate of flux accumulation inside the island ($E_{\text{Rec}} = \partial\Phi/\partial t$). (c) M component ($E_{\text{str},M}$) of the electric field from Magnetospheric Multiscale (MMS 1), MMS 2, and MMS 3 that made reliable electric field measurements, transformed into the frame commoving with the structure (see Text S3 in Supporting Information S1 for details), along with E_{Rec}. The upper and lower levels of the error bars are based on results from the EMHD reconstructions with an offset of $B_z = +0.1$ nT or -0.1 nT in GSE added to the measurements, considering that the error in the magnetic field measurements is ~0.1 nT (Russell et al., 2016). The flux values from the polynomial reconstruction are shown only when both the X- and O-points are within twice the spacecraft separation of the centroid of the MMS spacecraft, based on results by Denton et al. (2021).

Despite the slow growth of the island, the energy-conversion rate $\mathbf{j} \cdot \mathbf{E}' = \mathbf{j}_\text{p} \cdot (\mathbf{E} + \mathbf{v}_\text{e} \times \mathbf{B})$ (Zenitani et al., 2011; Figure 5e), where the particle current density is $\mathbf{j}_\text{p} = en_\text{e}(\mathbf{v}_\text{i} - \mathbf{v}_\text{e})$ with the elementary charge of e and $\mathbf{E}$ the electric field measured in the spacecraft frame, is strongly positive around an X-point closer to the center of the reconstruction domain. Its magnitude (~0.5 nW m^{-3}) is comparable to the value (~0.2 nW m^{-3}) expected for fast collisionless reconnection, based on the current density ~150 nA m^{-2} (Figure 2h) and reconnection electric field ~1.3 mV m^{-1} for $B \approx 15$ nT and inflow ion speed of $\sim 0.1 V_{\text{iA}} \approx 85$ km s^{-1} (Figure 2b). We thus conclude that energy conversion at the X-point was ongoing. Note that the active X-point was captured inside the MMS tetrahedron during the ECS crossing (Figures 5a–5d, 5g, and 5h), reinforcing the conclusions based on the reconstruction results.

In order to reveal how fast the magnetic island was growing, we calculated the amount of in-plane magnetic flux per unit length along $\mathbf{M}$ embedded between the reconstructed X- and O-points closer to the center of the reconstruction domain. Three cases are shown in Figure 6, one from the polynomial reconstruction and two from the EMHD reconstruction (see the caption of Figure 6 and Text S3 in Supporting Information S1 for details). Consistent with the island growth, the flux increases with time for all three cases (Figure 6a) and the measured component of the electric field along $\mathbf{M}$ (E_M) appears to vary in space and time (Figure 6c). However, the estimated rates of flux accumulation inside the island (E_{Rec} in Figure 6b) are about one order of magnitude smaller than the measured E_M (flux injection rate) that is comparable to the expected reconnection electric field of ~1.3 mV m^{-1}. Tests of our reconstruction methods using simulated data show that the estimated fluxes may differ by a factor of 4 at most (Figure S3, Texts S2 and S3 in Supporting Information S1). Thus, the result suggests that the in-plane magnetic field injected into the ECS was not ejected out of the X-point into the island, but annihilated around the X-point or O-point at the time and portion of the ECS observed by MMS. The small E_{Rec} inside the island (Figure 6) also indicates that the time evolution of the island was indeed slow, ensuring that the assumption of time-independence made in the EMHD reconstruction was approximately satisfied.

Since the reconstructed X-point may still be moving in the chosen structure frame, as suggested from Figures 5a–5d, we estimate how much the electric field $\mathbf{E}_X$ in the frame of strictly stationary X-point may differ from $\mathbf{E}_{\text{str}}$ (Figure 6c). Figures 5a–5d suggest that the X-point moved $\lesssim 30$ km roughly in the L direction during the ~0.4 s interval of the ECS crossing by the four spacecraft (Figure 2e), indicating that the X-point speed in the structure frame was $\lesssim 100$ km s^{-1}. Since $|B_N| \lesssim 1$ nT for the reconstructed interval (Figure 2g), the estimated magnitude of the difference between $E_{\text{str},M}$ and $E_{X,M}$ is $|\Delta E_M| \lesssim 0.1$ mV m^{-1}. This is much smaller than the measured $E_{\text{str},M} \gtrsim 1.0$ mV m^{-1}, so that our conclusion that the flux accumulation rate inside the island (Figure 6b) was about one order of magnitude smaller than the flux injection rate is not affected.

4. Theoretical Analysis

Is fast annihilation of the magnetic field as detected by MMS physically possible in an ECS? For quasi-steady 2-D reconnection in collisionless plasmas, electron demagnetization (violation of the electron frozen-in condition) at the X-line occurs when off-diagonal terms of the electron pressure tensor are significant (Hesse et al., 2011). Consistently, nongyrotropic electron velocity distributions as a manifestation of electron demagnetization have been observed in the present (Li et al., 2019) as well as other EDRs (Burch et al., 2016; Torbert et al., 2018). Earlier studies also demonstrated that the nongyrotropic electron pressure term can quantitatively account for the electric field (E_M) of fast reconnection as observed (Egedal et al., 2019). Here, we demonstrate that magnetic-field
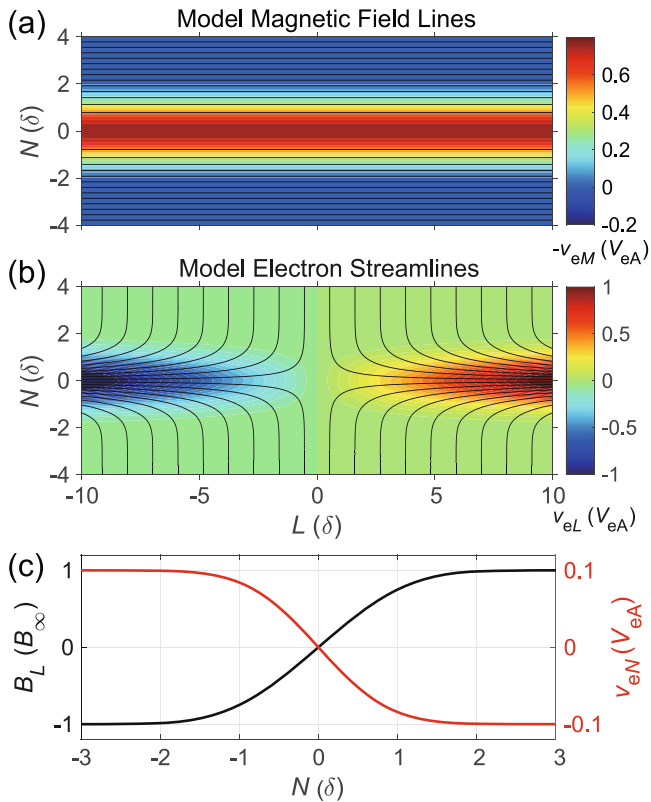
Figure 7. Exact solution of the dissipative electron-magnetohydrodynamics equations (Sonnerup et al., 2016) showing the magnetic field and electron velocity profiles in and around an electron-scale current sheet (ECS) with a thickness (δ) comparable to d_e. (a) Magnetic field-lines in the L–N plane with the out-of-plane ($-M$) component of the electron velocity in unit of V_{eA} in color. (b) Electron streamlines with the L component (v_{eL}) of the electron velocity in color. (c) Spatial profiles along **N** of v_{eN} and B_L in unit of the field intensity (B_∞) outside of the ECS.

annihilation may occur across **N** in an ECS extended in the L direction with $\partial/\partial M = 0$, when the generalized Ohm's law is expressed by

$$\mathbf{E} = -\mathbf{v}_e \times \mathbf{B} + \frac{f(L, N)}{n_e e}\mathbf{M}. \tag{1}$$

Note that Equation 1 has been used in the inertia-less version of the EMHD method (Sonnerup et al., 2016) with the following expression

$$f(L, N) = n_e \sqrt{2 m_e k_B T_e} \frac{\partial v_{eL}}{\partial L}, \tag{2}$$

and Hesse et al. (2011) and Kuznetsova et al. (2007) have shown that Equation 2 is applicable to the diffusion region of antiparallel reconnection.

We consider Faraday's law in the LMN coordinate system,

$$\frac{\partial \mathbf{B}}{\partial t} = -\nabla \times \mathbf{E} = \nabla \times (\mathbf{v}_e \times \mathbf{B}) - \frac{1}{n_e e}\nabla f(L, N) \times \mathbf{M}, \tag{3}$$

and discuss only the contribution of the second term on the right-hand side (RHS) of Equation 3, because the first term does not violate the electron frozen-in condition. Furthermore, only the L component

$$\frac{\partial B_L}{\partial t} \approx \frac{1}{n_e e}\frac{\partial f(L, N)}{\partial N} \tag{4}$$

is considered, because $B_N \approx 0$ in ECSs elongated in the L direction. Since constant electron density, namely incompressible electron fluid ($\nabla \cdot \mathbf{v}_e = \partial v_{eL}/\partial L + \partial v_{eN}/\partial N = 0$), can be assumed in EDRs (Hesse et al., 2011; Sonnerup et al., 2016), the following relation results using Equation 2

$$\frac{\partial B_L}{\partial t} \approx -\frac{\sqrt{2 m_e k_B T_e}}{e}\frac{\partial^2 v_{eN}}{\partial N^2}. \tag{5}$$

We note that a relation $-B_\infty v_{eN} \approx B_L V_\infty$ is approximately satisfied inside an EDR because the spatial variations along **N** of B_L and v_{eN} are very similar to each other with only sign difference (Figure 7), while in the inflow region outside of the EDR $|B_L v_{eN}| \approx E_0 = B_\infty V_\infty$ holds for quasi-steady 2-D reconnection (Liu et al., 2017). Here, E_0 is the reconnection electric field, and B_∞ and V_∞ are the B_L intensity and the electron inflow speed, respectively, immediately outside of the EDR, with $V_\infty \approx 0.1 V_{eA}$ for fast reconnection where the electron Alfvén speed $V_{eA} = B_\infty/(\mu_0 m_e n_e)^{1/2}$. Thus, the above relation becomes a diffusion equation for B_L

$$\frac{\partial B_L}{\partial t} \approx D_B \frac{\partial^2 B_L}{\partial N^2}, \tag{6}$$

where the diffusion coefficient $D_B = r_{ge} V_\infty$ with gyroradius of thermal electrons $r_{ge} = (2 m_e k_B T_e)^{1/2}/(e B_\infty)$. We can therefore conclude that in the presence of the term (2), equivalent to the nongyrotropic electron pressure tensor term, the in-plane magnetic-field component B_L may be annihilated in an EDR, as long as the EDR thickness is of electron scale. This conclusion is consistent with the theoretical analysis (Hesse et al., 2011) in which the term (2) was derived by discussing a diffusion of the electron current density j_{eM} that implies the annihilation of B_L. On the other hand, since the second term on the RHS of Equation 3 has no M component, no annihilation of B_M (Hall magnetic field) occurs for 2-D reconnection. Moreover, the form of D_B indicates that in principle fast magnetic-field annihilation may occur when fast inflow of the in-plane magnetic flux exists.

The B_L diffusion implied by Equation 6 is consistent with an exact solution of the EMHD equations with the dissipation term (2) for a steady ECS, derived by Sonnerup et al. (2016), for which the inflowing B_L is all annihi-
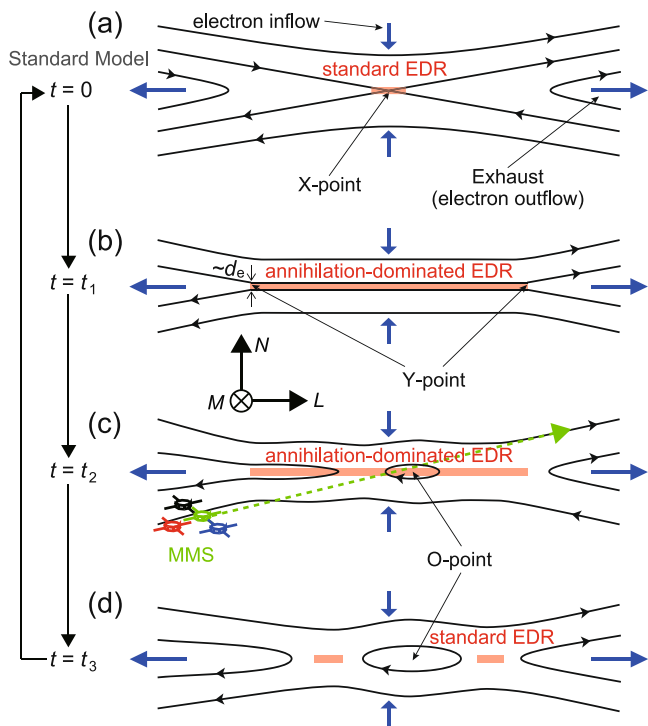
Figure 8. Possible sequence of time evolution of the electron-scale current sheet observed by Magnetospheric Multiscale (MMS) on 10 August 2017. (a) Standard electron diffusion region (EDR) with an X-type magnetic field geometry where the magnetic-to-particle energy conversion is mostly due to magnetic topology change (Torbert et al., 2018). (b) EDR after elongation along L, as seen in kinetic simulations (Daughton et al., 2006, Figure 1), where the energy conversion may be mostly due to magnetic field annihilation (Section 4; see also Nakamura et al., 2021). (c) Initial stage of the magnetic island formation in the EDR, as observed by MMS. (d) Possible later stage of the island growth in exhausts of the EDRs, as seen in simulations (Figure 1).

lated rather than reconnected in the EDR (Figure 7). We can experimentally estimate the diffusion coefficient $D_{B,\exp}$ assuming that the magnetic structure is quasi-steady so that the diffusion and convection terms are canceled out, that is, the RHS of Equation 6 is equal to the L component of the first term on the RHS of Equation 3. For the observed ECS with a thickness $\delta \approx d_e$, the estimated coefficient $D_{B,\exp} \approx \delta V_\infty = d_e E_{str,M} / B_\infty \sim 5 \times 10^9 \text{ m}^2\text{s}^{-1}$, which is comparable to the theoretically predicted coefficient $D_B = r_{ge} V_\infty \sim 10^{10} \text{ m}^2\text{s}^{-1}$ because the observed electron beta $\beta_e = r_{ge}^2 / d_e^2 \sim 5$.

The fast collisionless annihilation is in stark contrast with annihilation in the classic (resistive magnetohydrodynamics) model (Parker, 1957; Sweet, 1958) of reconnection in an elongated current sheet that is negligible under magnetotail conditions. However, we do not exclude a likely possibility that at the sunward and anti-sunward ends of the present ECS, where the magnetic field may have had a Y-type geometry (Figures 8b and 8c), the magnetic field was efficiently reconnected and ejected downstream, as observed for other magnetotail reconnection events (Nakamura et al., 2018).

5. Summary and Discussion

The main results of our study can be summarized as follows. (a) The MMS observations reported in the present paper are consistent with fast energy conversion in an elongated EDR dominated by magnetic field annihilation (Figure 8); (b) the fully kinetic simulation shows annihilation-dominated energy conversion in and around electron-scale islands formed in the EDR elongated in the exhaust direction (Figure 1); and (c) theoretical analysis suggests that fast collisionless magnetic diffusion can occur in a planar EDR with nongyrotropic electrons (Section 4). Thus, three different approaches, namely, our MMS event analysis, simulation, and theoretical analysis all support magnetic field annihilation in an elongated EDR. The discovery of the annihilation in a reconnecting ECS could have far-reaching implications for how magnetic energy is dissipated in plasma turbulence in the collisionless regime, because reconnection has been suggested to play a role in the dissipation process (Matthaeus & Lamkin, 1986; Retinò et al., 2007; Servidio et al., 2009).

The collisionless annihilation on the electron scale may not be surprising; the annihilation observed in the present event is probably an aspect of standard collisionless reconnection when the EDR is elongated. We note, however, that no earlier study has shown that its signatures are identifiable. This is probably because observable signatures are nearly the same as in the case of standard EDR geometry if an observing probe is located in regions outside of the EDR or downstream of the Y-points (Figures 8b and 8c).

An important question remains about whether the magnetic energy dissipated by the annihilation is partitioned to thermal or nonthermal electrons, if not to the electron bulk flow. Recently, Nakamura et al. (2021) have shown, based on a fully kinetic simulation, that electrons are strongly heated in electron-scale magnetic islands where the annihilation is ongoing. In the present event, however, no clear signature of electron heating or energization was identified, likely because electron beta β_e outside the EDR was so high ($\sim$5) that available magnetic energy was probably too small for energization effects to be identified; even if all the magnetic energy was converted to electron thermal energy, the temperature increase would be only about 20% of the ambient value. It is noted that for typical reconnection, only $\sim$2% of the available magnetic energy is partitioned to thermal electrons in reconnection exhausts (Phan et al., 2013). Thus, the process of energy partition through the annihilation will need to be quantitatively assessed in the future.

We point out that even without magnetic topology change and only with magnetic field annihilation, fast electron flows can be generated self-consistently (see Figure 2 of Sonnerup et al. (2016)). This is because under incompressible conditions, electron thermal energy may soon be converted to electron bulk-flow energy, that is, local increase of the electron temperature through magnetic field annihilation, leading to local buildup of the electron pressure (pressure gradient), may immediately accelerate electrons, resulting in electron bulk flows. The present MMS event was a nearly incompressible case with roughly constant density (Figure 2i) because the electron flow speed in the L–N plane ($|V_{eL}| \sim 5000$ km s^{-1} at maximum in Figures 2c and 2j) was significantly smaller than both the electron Alfvén speed ($V_{eA} \sim 10000$ km s^{-1}) and thermal velocity (~ 20000 km s^{-1}) for most of the time. This may also be a reason for no electron heating or energization signature.

Another intriguing observational feature worth noting is a displacement along the outflow direction of the X-point and electron stagnation point, as revealed by Hasegawa et al. (2019, 2021), for an MMS magnetotail EDR event reported by Torbert et al. (2018). It suggests that particle motion under prescribed electromagnetic field (Speiser, 1965) may not be the only factor controlling the electron bulk flow in and around the EDR, and electron hydrodynamic (collective) effects may also be important. This is the concept compatible with the fast electron flow generation from magnetic field annihilation, discussed in the previous paragraph.

One may raise the possibility that the elongation of the EDR is rare or the length of the elongated EDR is only a few times that of standard EDR at most, so that the annihilation would not have any significant impact. This may be the case in situations where reconnection occurs spontaneously. However, ECSs can be generated frequently or at many locations in turbulent plasma or through flow shear instabilities (Nakamura et al., 2013), and an integrated effect of the annihilation in such ECSs may not be negligible. On the other hand, the elongated EDR is unstable to the formation of electron-scale magnetic islands (Nakamura et al., 2021), so that the annihilation may only be a transient process, in contrast to the steady-state solution as shown in Figure 7. Both the simulation (Figure 1) and observations (Section 3.5) suggest that the annihilation may last for about one ion cyclotron period for each cycle of electron-scale island formation.

We cannot rule out the possibility that the reconnected fluxes may be transferred away from the observation site in the X line direction under 3-D effects. However, the MDD results (Figure 3f) show that the ECS was nearly one-dimensional over the EMHD reconstruction interval (1.9 s). Considering that the average field line convection velocity along the X line direction was $\langle v_{ExBM} \rangle = -1620$ km s^{-1} (Figure 2j), we estimate that the structure may have moved $\sim 5d_i$ (3077 km) in the $-\mathbf{M}$ direction during the 1.9 s interval. Thus, if 3-D effects were responsible for our observations, the flux removal in that direction must have occurred on the scale comparable to or larger than $\sim 5d_i$. Figure 2j also shows that $|v_{ExBM}|$ is not significantly larger than $|v_{ExBL}|$ around the center of the ECS, which is consistent with no strong flux transfer along the X line direction.

Although 3-D effects appear to be weak in the present EDR event, such effects may be important in other magnetotail events as reported by Ergun et al. (2018). In their event, current sheet crossing was observed 6 times only during a 1.5 min interval (see the right panel of their Figure 1), while in the present event only two crossings were observed during a 1.5 min period 12:18:00–12:19:30 UT (Figure 2a). Such multiple current sheet crossings during a short interval suggest an undulating current sheet, as seen in a 3-D simulation reported by Fujimoto and Cao (2021). Transient energy conversions and a flux rope-like feature reported by Ergun et al. (2018) may be consistent with their 3-D simulation. A challenging problem is to observationally understand how the dissipation of magnetic energy occurs in the presence of significant 3-D effects.

While the present observations and theory have shown that magnetic field annihilation can occur in a high β_e ECS across which the magnetic fields are nearly antiparallel, it remains unknown whether the annihilation can occur under low β_e and significant guide field conditions when electrons are magnetized more strongly. This is because the dissipation term (2) may not be applicable to guide field cases and the diffusion coefficient $D_B = r_{ge}V_\infty$ in Equation 6 becomes small under low β_e or small r_{ge} conditions. Since guide-field reconnection is quite common in the solar wind (Vasko et al., 2021) and magnetosheath (Phan et al., 2018), and reconnection in the solar corona or inner heliosphere can occur under low beta conditions, it would be worthwhile to explore the properties of the collisionless annihilation under more general conditions.

Data Availability Statement

All MMS data used in this study are publicly available via the MMS Science Data Center at https://lasp.colorado.edu/mms/sdc/public/about/browse-wrapper/. All codes used to analyze the MMS data in this study are based on the publicly available SPEDAS tools (Angelopoulos et al., 2019) (http://spedas.org/downloads/spedas_5_0.zip), except for the Matlab code for the EMHD and polynomial reconstructions. The Matlab code for the EMHD reconstruction can be found at the Zenodo (https://doi.org/10.5281/zenodo.5144478), and that for the polynomial reconstruction at https://doi.org/10.5281/zenodo.3906853.

References

Angelopoulos, V., Cruce, P., Drozdov, A., Grimes, E. W., Hatzigeorgiu, N., King, D. A., et al. (2019). The space physics environment data analysis system (SPEDAS). *Space Science Reviews*, *215*(1), 9. https://doi.org/10.1007/s11214-018-0576-4

Angelopoulos, V., McFadden, J. P., Larson, D., Carlson, C. W., Mende, S. B., Frey, H., et al. (2008). Tail reconnection triggering substorm onset. *Science*, *321*(5891), 931–935. https://doi.org/10.1126/science.1160495

Burch, J. L., Torbert, R. B., Phan, T. D., Chen, L. J., Moore, T. E., Ergun, R. E., et al. (2016). Electron-scale measurements of magnetic reconnection in space. *Science*, *352*(6290), aaf2939. https://doi.org/10.1126/science.aaf2939

Daughton, W., Scudder, J., & Karimabadi, H. (2006). Fully kinetic simulations of undriven magnetic reconnection with open boundary conditions. *Physics of Plasmas*, *13*(7), 072101. https://doi.org/10.1063/1.2218817

Denton, R. E., Sonnerup, B. U. Ö., Hasegawa, H., Phan, T. D., Russell, C. T., Strangeway, R. J., et al. (2016). Motion of the MMS spacecraft relative to the magnetic reconnection structure observed on 16 Oct 2015 at 1307 UT. *Geophysical Research Letters*, *43*(11), 5589–5596. https://doi.org/10.1002/2016GL069214

Denton, R. E., Sonnerup, B. U. Ö., Russell, C. T., Hasegawa, H., Phan, T. D., Strangeway, R. J., et al. (2018). Determining L-M-N current sheet coordinates at the magnetopause from magnetospheric multiscale data. *Journal of Geophysical Research: Space Physics*, *123*, 2274–2295. https://doi.org/10.1002/2017JA024619

Denton, R. E., Torbert, R. B., Hasegawa, H., Dors, I., Genestreti, K. J., Argall, M. R., et al. (2020). Polynomial reconstruction of the reconnection magnetic field observed by multiple spacecraft. *Journal of Geophysical Research: Space Physics*, *125*(2), e2019JA027481. https://doi.org/10.1029/2019JA027481

Denton, R. E., Torbert, R. B., Hasegawa, H., Genestreti, K. J., Manuzzo, R., Belmont, G., et al. (2021). Two-dimensional velocity of the magnetic structure observed on 11 July 2017 by the Magnetospheric Multiscale spacecraft. *Journal of Geophysical Research: Space Physics*, *126*(3), e2020JA028705. https://doi.org/10.1029/2020JA028705

Dunlop, M. W., Balogh, A., Glassmeier, K.-H., & Robert, P. (2002). Four-point cluster application of magnetic field analysis tools: The curlometer. *Journal of Geophysical Research*, *107*(A11), 1384. https://doi.org/10.1029/2001JA005088

Egedal, J., Ng, J., Le, A., Daughton, W., Wetherton, B., Dorelli, J., et al. (2019). Pressure tensor elements breaking the frozen-in law during reconnection in Earth's magnetotail. *Physical Review Letters*, *123*(22), 225101. https://doi.org/10.1103/PhysRevLett.123.225101

Ergun, R. E., Goodrich, K. A., Wilder, F. D., Ahmadi, N., Holmes, J. C., Eriksson, S., et al. (2018). Magnetic reconnection, turbulence, and particle acceleration: Observations in the Earth's magnetotail. *Geophysical Research Letters*, *45*(8), 3338–3347. https://doi.org/10.1002/2018GL076993

Ergun, R. E., Tucker, S., Westfall, J., Goodrich, K. A., Malaspina, D. M., Summers, D., et al. (2016). The axial double probe and fields signal processing for the MMS mission. *Space Science Reviews*, *199*(1–4), 167–188. https://doi.org/10.1007/s11214-014-0115-x

Fujimoto, K. (2006). Time evolution of the electron diffusion region and the reconnection rate in fully kinetic and large system. *Physics of Plasmas*, *13*(7), 072904. https://doi.org/10.1063/1.2220534

Fujimoto, K., & Cao, J.-B. (2021). Non-adiabatic electron heating in the magnetic islands during magnetic reconnection. *Geophysical Research Letters*, *48*(19), e2021GL094431. https://doi.org/10.1029/2021GL094431

Hasegawa, H., Denton, R. E., Nakamura, R., Genestreti, K. J., Nakamura, T. K. M., Hwang, K., et al. (2019). Reconstruction of the electron diffusion region of magnetotail reconnection seen by the MMS spacecraft on 11 July 2017. *Journal of Geophysical Research: Space Physics*, *124*(1), 122–138. https://doi.org/10.1029/2018JA026051

Hasegawa, H., Nakamura, T. K. M., & Denton, R. E. (2021). Reconstruction of the electron diffusion region with inertia and compressibility effects. *Journal of Geophysical Research: Space Physics*, *126*(11), e2021JA029841. https://doi.org/10.1029/2021JA029841

Hesse, M., Neukirch, T., Schindler, K., Kuznetsova, M., & Zenitani, S. (2011). The diffusion region in collisionless magnetic reconnection. *Space Science Reviews*, *160*(1–4), 3–23. https://doi.org/10.1007/s11214-010-9740-1

Jain, N., & Sharma, A. S. (2015). Evolution of electron current sheets in collisionless magnetic reconnection. *Physics of Plasmas*, *22*(10), 102110. https://doi.org/10.1063/1.4933120

Kawano, H., & Higuchi, T. (1995). The bootstrap method in space physics: Error estimation for minimum variance analysis. *Geophysical Research Letters*, *22*(3), 307–310. https://doi.org/10.1029/94GL02969

Kuznetsova, M. M., Hesse, M., Rastaetter, L., Taktakishvili, A., Toth, G., De Zeeuw, D. L., et al. (2007). Multiscale modeling of magnetospheric reconnection. *Journal of Geophysical Research*, *112*(A10), A10210. https://doi.org/10.1029/2007JA012316

Li, X., Wang, R., Lu, Q., Hwang, K., Zong, Q., Russell, C. T., & Wang, S. (2019). Observation of nongyrotropic electron distribution across the electron diffusion region in the magnetotail reconnection. *Geophysical Research Letters*, *46*(24), 14263–14273. https://doi.org/10.1029/2019GL085014

Lindqvist, P.-A., Olsson, G., Torbert, R. B., King, B., Granoff, M., Rau, D., et al. (2016). The Spin-plane Double Probe electric field instrument for MMS. *Space Science Reviews*, *199*(1–4), 137–165. https://doi.org/10.1007/s11214-014-0116-9

Liu, Y.-H., Hesse, M., Guo, F., Daughton, W., Li, H., Cassak, P., & Shay, M. (2017). Why does steady-state magnetic reconnection have a maximum local rate of order 0.1? *Physical Review Letters*, *118*(8), 085101. https://doi.org/10.1103/PhysRevLett.118.085101

Matthaeus, W. H., & Lamkin, S. L. (1986). Turbulent magnetic reconnection. *Physics of Plasmas*, *29*(8), 2513–2534. https://doi.org/10.1063/1.866004

Nagai, T., Shinohara, I., Fujimoto, M., Hoshino, M., Saito, Y., Machida, S., & Mukai, T. (2001). Geotail observations of the Hall current system: Evidence of magnetic reconnection in the magnetotail. *Journal of Geophysical Research*, *106*(A11), 25929–25949. https://doi.org/10.1029/2001ja900038

Nagai, T., Shinohara, I., Fujimoto, M., Matsuoka, A., Saito, Y., & Mukai, T. (2011). Construction of magnetic reconnection in the near-Earth magnetotail with geotail. *Journal of Geophysical Research*, *116*(A4), A04222. https://doi.org/10.1029/2010JA016283

Nakamura, T. K. M., Daughton, W., Karimabadi, H., & Eriksson, S. (2013). Three-dimensional dynamics of vortex-induced reconnection and comparison with THEMIS observations. *Journal of Geophysical Research: Space Physics*, *118*(9), 5742–5757. https://doi.org/10.1002/jgra.50547

Nakamura, T. K. M., Genestreti, K. J., Liu, Y.-H., Nakamura, R., Teh, W., Hasegawa, H., et al. (2018). Measurement of the magnetic reconnection rate in the Earth's magnetotail. *Journal of Geophysical Research: Space Physics*, *123*(11), 9150–9168. https://doi.org/10.1029/2018JA025713

Nakamura, T. K. M., Hasegawa, H., Genestreti, K. J., Denton, R. E., Phan, T. D., Stawarz, J. E., et al. (2021). Fast cross-scale energy transfer during turbulent magnetic reconnection. *Geophysical Research Letters*, *48*(13), e2021GL093524. https://doi.org/10.1029/2021GL093524

Øieroset, M., Phan, T. D., Fujimoto, M., Lin, R. P., & Lepping, R. P. (2001). In situ detection of collisionless reconnection in the Earth's magnetotail. *Nature*, *412*(6845), 414–417. https://doi.org/10.1038/35086520

Parker, E. N. (1957). Sweet's mechanism for merging magnetic fields in conducting fluids. *Journal of Geophysical Research*, *62*(4), 509–520. https://doi.org/10.1029/jz062i004p00509

Phan, T. D., Eastwood, J. P., Shay, M. A., Drake, J. F., Sonnerup, B. U. Ö., Fujimoto, M., et al. (2018). Electron magnetic reconnection without ion coupling in Earth's turbulent magnetosheath. *Nature*, *557*(7704), 202–206. https://doi.org/10.1038/s41586-018-0091-5

Phan, T. D., Shay, M. A., Gosling, J. T., Fujimoto, M., Drake, J. F., Paschmann, G., et al. (2013). Electron bulk heating in magnetic reconnection at Earth's magnetopause: Dependence on the inflow Alfven speed and magnetic shear. *Geophysical Research Letters*, *40*(17), 4475–4480. https://doi.org/10.1002/grl.50917

Pollock, C., Moore, T., Jacques, A., Burch, J., Gliese, U., Saito, Y., et al. (2016). Fast plasma investigation for magnetospheric Multiscale. *Space Science Reviews*, *199*(1–4), 331–406. https://doi.org/10.1007/s11214-016-0245-4

Retinò, A., Sundkvist, D., Vaivads, A., Mozer, F., André, M., & Owen, C. J. (2007). In situ evidence of magnetic reconnection in turbulent plasma. *Nature Physics*, *3*(4), 235–238. https://doi.org/10.1038/nphys574

Rezeau, L., Belmont, G., Manuzzo, R., Aunai, N., & Dargent, J. (2018). Analyzing the magnetopause internal structure: New possibilities offered by MMS tested in a case study. *Journal of Geophysical Research: Space Physics*, *123*(1), 227–241. https://doi.org/10.1002/2017JA024526

Russell, C. T., Anderson, B. J., Baumjohann, W., Bromund, K. R., Dearborn, D., Fischer, D., et al. (2016). The magnetospheric Multiscale magnetometers. *Space Science Reviews*, *199*(1–4), 189–256. https://doi.org/10.1007/s11214-014-0057-3

Servidio, S., Matthaeus, W. H., Shay, M. A., Cassak, P. A., & Dmitruk, P. (2009). Magnetic reconnection in two-dimensional magnetohydrodynamic turbulence. *Physical Review Letters*, *102*(11), 115003. https://doi.org/10.1103/physrevlett.102.115003

Shay, M. A., Drake, J. F., & Swisdak, M. (2007). Two-scale structure of the electron dissipation region during collisionless magnetic reconnection. *Physical Review Letters*, *99*(15), 155002. https://doi.org/10.1103/PhysRevLett.99.155002

Shi, Q. Q., Tian, A. M., Bai, S. C., Hasegawa, H., Degeling, A. W., Pu, Z. Y., et al. (2019). Dimensionality, coordinate system and reference frame for analysis of in-situ space plasma and field data. *Space Science Reviews*, *215*(4), 35. https://doi.org/10.1007/s11214-019-0601-2

Sonnerup, B. U. Ö., Hasegawa, H., Denton, R. E., & Nakamura, T. K. M. (2016). Reconstruction of the electron diffusion region. *Journal of Geophysical Research: Space Physics*, *121*(5), 4279–4290. https://doi.org/10.1002/2016JA022430

Sonnerup, B. U. Ö., & Scheible, M. (1998). Minimum and maximum variance analysis. In G. Paschmann & P. W. Daly (Eds.), *Analysis methods for multi-spacecraft data* (pp. 185–220). ISSI/ESA. chap. 8.

Speiser, T. W. (1965). Particle trajectories in model current sheets: 1. Analytical solutions. *Journal of Geophysical Research*, *70*(17), 4219–4226. https://doi.org/10.1029/JZ070i017p04219

Sweet, P. A. (1958). The neutral point theory of solar flares. In B. Lehnert (Ed.), *Electromagnetic Phenomena in Cosmical Physics* (pp. 123–134). https://doi.org/10.1017/s0074180900237704

Torbert, R. B., Burch, J. L., Phan, T. D., Hesse, M., Argall, M. R., Shuster, J., et al. (2018). Electron-scale dynamics of the diffusion region during symmetric magnetic reconnection in space. *Science*, *362*(6421), 1391–1395. https://doi.org/10.1126/science.aat2998

Torbert, R. B., Russell, C. T., Magnes, W., Ergun, R. E., Lindqvist, P. A., LeContel, O., et al. (2016). The FIELDS instrument suite on MMS: Scientific objectives, measurements, and data products. *Space Science Reviews*, *199*(1–4), 105–135. https://doi.org/10.1007/s11214-014-0109-8

Vasko, I. Y., Alimov, K., Phan, T. D., Bale, S. D., Mozer, F. S., & Artemyev, A. V. (2021). Kinetic-scale current sheets in the solar wind at 1 au: Properties and the necessary condition for reconnection. *The Astrophysical Journal Letters*, *923*, L19. https://doi.org/10.3847/2041-8213/ac3f30

Zenitani, S., Hesse, M., Klimas, A., & Kuznetsova, M. (2011). New measure of the dissipation region in collisionless magnetic reconnection. *Physical Review Letters*, *106*(19), 195003. https://doi.org/10.1103/PhysRevLett.106.195003

Zhou, M., Deng, X. H., Zhong, Z. H., Pang, Y., Tang, R. X., El-Alaoui, M., et al. (2019). Observations of an electron diffusion region in symmetric reconnection with weak guide field. *The Astrophysical Journal*, *870*(1), 34. https://doi.org/10.3847/1538-4357/aaf16f

References From the Supporting Information

Hasegawa, H., Sonnerup, B. U. Ö., Denton, R. E., Phan, T.-D., Nakamura, T. K. M., Giles, B. L., et al. (2017). Reconstruction of the electron diffusion region observed by the Magnetospheric Multiscale spacecraft: First results. *Geophysical Research Letter*, *44*, 4566–4574. https://doi.org/10.1002/2017GL073163

Nakamura, T. K. M., Stawarz, J. E., Hasegawa, H., Narita, Y., Franci, L., Wilder, F. D., et al. (2020). Effects of fluctuating magnetic field on the growth of the Kelvin-Helmholtz instability at the Earth's magnetopause. *Journal of Geophysical Research: Space Physics*, *125*, e2019JA027515. https://doi.org/10.1029/2019JA027515

Torbert, R. B., Dors, I., Argall, M. R., Genestreti, K. J., Burch, J. L., Farrugia, C. J., et al. (2020). A new method of 3-D magnetic field reconstruction. *Geophysical Research Letter*, *47*, e2019GL085542. https://doi.org/10.1029/2019GL085542